LAWRENCE
LIVERMORE
NATIONAL
LABORATORY

LLNL-JRNL-827019

Quantifying Spatial Resolution in a Fast Neutron Radiography System

I. Oksuz, M. Bisbee, J. Hall, N. Cherepy, L. Cao

September 23, 2021

Nuclear Instruments and Methods A

Disclaimer

This document was prepared as an account of work sponsored by an agency of the United States government. Neither the United States government nor Lawrence Livermore National Security, LLC, nor any of their employees makes any warranty, expressed or implied, or assumes any legal liability or responsibility for the accuracy, completeness, or usefulness of any information, apparatus, product, or process disclosed, or represents that its use would not infringe privately owned rights. Reference herein to any specific commercial product, process, or service by trade name, trademark, manufacturer, or otherwise does not necessarily constitute or imply its endorsement, recommendation, or favoring by the United States government or Lawrence Livermore National Security, LLC. The views and opinions of authors expressed herein do not necessarily state or reflect those of the United States government or Lawrence Livermore National Security, LLC, and shall not be used for advertising or product endorsement purposes.

Quantifying Spatial Resolution in a Fast Neutron Radiography System

Ibrahim Oksuz[1], Matt Bisbee[1], James Hall[3], Nerine Cherepy[3], and Lei Cao[1,2*]

[1]Nuclear Engineering Program, Department of Mechanical and Aerospace Engineering, The Ohio State University, Columbus, Ohio 43210, USA.

[2]Nuclear Reactor Laboratory, College of Engineering, The Ohio State University, Columbus, Ohio 43210, USA.

[3] Lawrence Livermore National Laboratory Livermore, California 94550, USA

*cao.152@osu.edu

ABSTRACT

Neutron imaging is a powerful nondestructive examination modality that has been employed in various applications. Fast neutrons provide advantages over lower energy neutrons, such as examining thicker samples and inducing negligible activation and transmutations. However, fast neutrons interact mostly via elastic scattering with both the neutron detector and the object, causing degradation in spatial resolution. This study explores the quantification of spatial resolution caused by the testing target itself and suggests proper candidate materials for characterizing spatial resolution in terms of modulation transfer function. Knife-edge radiographs of 3 mm, 6 mm, and 5 cm thick Tantalum (Ta) foils, and a 2.54 cm Tungsten (W) cube were acquired using a CCD-based imaging system and a Polyvinyl Toluene (PVT) scintillator at the Ohio State Research Reactor (OSURR)'s fast neutron beam facility. The spatial resolutions calculated were 195 ± 20 μm, 224 ± 22 μm, 248 ± 25 μm, and 435 ± 44 μm for 3 mm, 6 mm, and 5 cm Ta foils, and 2.54

cm W cube, respectively. The results showed a worsening spatial resolution with increasing target thickness. Simulations and calculations estimate that elastic scattering kinematics between neutrons and protons in the PVT medium also limits spatial resolution, and it sets a lower limit of ~44 μm on the spatial resolution for 2 MeV neutrons.

Keywords: Fast neutron, Spatial resolution, PVT scintillator, Neutron imaging, Neutron Scattering, Modulation transfer function

1. INTRODUCTION

Neutron imaging is being performed at facilities around the world, utilizing neutrons with energy spectra ranging from meV to MeV, *i.e.*, cold neutrons to fast neutrons [1-4]. The appropriate neutron energy must be selected for a given imaging application and will vary depending on the elemental constituents and size of the sample being investigated. Fast neutrons offer good penetration in large sized multi-material samples comprised of low-Z elements shielded within high-Z materials and samples comprised of denser materials (e.g., nuclear fuel). However, having a lower interaction probability, compared to X-rays, makes detection of fast neutrons and characterization of imaging performance challenging in fast neutron imaging applications.

Spatial resolution of a neutron imaging system is a multifaceted parameter that is effected by four major categories, including 1.) neutron source characteristics (spot size, collimation, Cadmium ratio), 2.) test targets (neutron capture vs scattering cross sections, target geometry and thickness), 3.) neutron detector (scintillator thickness, neutron capture and/or scattering cross section in the

scintillator, pixel size of camera or flat panel array), and 4.) optical components (mirror, lens, pixel size, dark current of a CCD camera) when the system is based on lens-coupled readout. Many of the archived studies for the spatial resolution of neutron imaging systems have quantified the contributions of these factors but are lacking significant consideration of the effects of test target itself on the overall spatial resolution. The neutron detection mechanism in a lithium enriched thermal neutron imager occurs via neutron capture reaction in which ^{6}Li disintegrates into two charged particles i.e., alpha particle and triton [5, 6]. The resulting charged particles lose energy as they travel in the thin scintillator medium, similar to the recoiled proton originating from the neutron-proton elastic scattering reaction losing energy in the PVT medium. Relatively high spatial resolution obtained in thermal or cold neutron imaging is due to the use of a low energy neutron beam with minimum scattering effects and a thin scintillator. At higher neutron energies, however, the spatial resolution starts degrading because the energy deposition mechanism changes from capture to scattering, and the thickness of the scintillator detector material needs to be increased to compensate for the decreasing interaction cross-section.

In terms of the optimal detector thickness in the fast neutron imaging, one study utilizing fission neutrons obtained a spatial resolution of 200 μm with 3 mm thick poly-ethylene (PE) on which a 0.06 mm thick ZnS:Ag is coated [7]. Polyvinyl Toluene (PVT) scintillators ranging from 3 mm to 10 mm with different emitting dopants were evaluated for optimized resolution and light yield using a reactor based fast neutron beam [8, 9]. Thin Gadolinium (Gd) or Cadmium (Cd) foils are normally used as testing targets in thermal (or cold) neutron imaging for their high thermal neutron capture cross-section (~257,000 barns for ^{157}Gd and ~48,000 for Gd), in which case the neutron capture dominates the attenuation, and the neutron scattering is negligible. Sufficient target

thickness is required to induce the detectable contrast in fast neutron imaging, but thick targets introduce an increased intrinsic scattering that complicates the knife edge methods for characterizing the system spatial resolution.

The main objective of this study is to explore the effect of thickness on spatial resolution for an imaging target with high scattering cross-section in fast neutron imaging. A collimated research reactor fast neutron beamline (divergence ~0.6°) and a Polyvinyl Toluene (PVT) based plastic scintillator are used in the study. For the test target, dense materials with high elastic scattering cross-section for fast neutrons, Tantalum (σ_{El}≈4.16 barns @ 2 MeV, ρ=16.65 g/cm3) and Tungsten (σ_{El}≈3.80 barns @ 2 MeV, ρ=19.3 g/cm^3) were selected. The acquired knife-edge radiograph was used to generate the modulation transfer function (MTF), which gives the spatial resolution of the overall imaging system [10, 11]. Additionally, this study investigates the impact of the interaction kinematics between neutrons and Hydrogen nuclei in the PVT detector material on spatial resolution.

2. EXPERIMENTAL

2.1 Beam Facility and Experimental Setup

MTF data were collected at the fast neutron beam facility of The Ohio State University Research Reactor (OSURR). The beam facility provides a collimated neutron beam with a geometric L/D ratio of ~62 (calculated from experimental data), a beam diameter of ~3.2 cm, and an MCNP simulated flux of ~5.4 x 10^7 n·cm^{-2}·s^{-1} at 1.6 MeV (median energy) at full reactor power of 500

kW [12]. A 2.54-cm thick lithiated glass was placed in the beam to remove thermal neutrons via the ^{6}Li (n, ^{4}He) ^{3}H thermal neutron capture reaction. Radiography data acquisition was performed employing a CCD-based imaging system, comprised of an Electron Multiplying (EM) Charged Coupled Device (CCD) camera cooled by water circulation to decrease thermal noise, and shielded with borated polyethylene sheets and lead bricks to lower the effect of neutrons and gamma rays on the CCD sensor, a light-tight apparatus, and a front surface mirror placed at 45° with respect to the incoming neutron beam, both to reflect scintillation lights onto the camera sensor and to prevent the camera being exposed directly in the neutron beam. A 1-cm thick high light yield (HiLY) Polyvinyl Toluene plastic scintillator, providing ~3X more light compared to a conventional PVT scintillator, doped with an Ir-complex fluor (FIracac), is shown in Figure 1. The scintillator, provided by Lawrence Livermore National Laboratory (LLNL), was used as a neutron detector [13, 14]. The back and edges of this scintillator were blackened to minimize optical scatter. Additionally, a rotation stage was utilized to rotate foils, placed on a wooden holder attached to the rotation stage, to align the edge of the foil with the scintillator and the beam. A linear XYZ stage was employed to adjust the foil position with respect to the scintillator. Figure 1 provides a depiction of the experimental setup, as well as photographs of the rotation stage as the 6 mm thick Ta foil being set on the wooden holder and partial experimental setup.

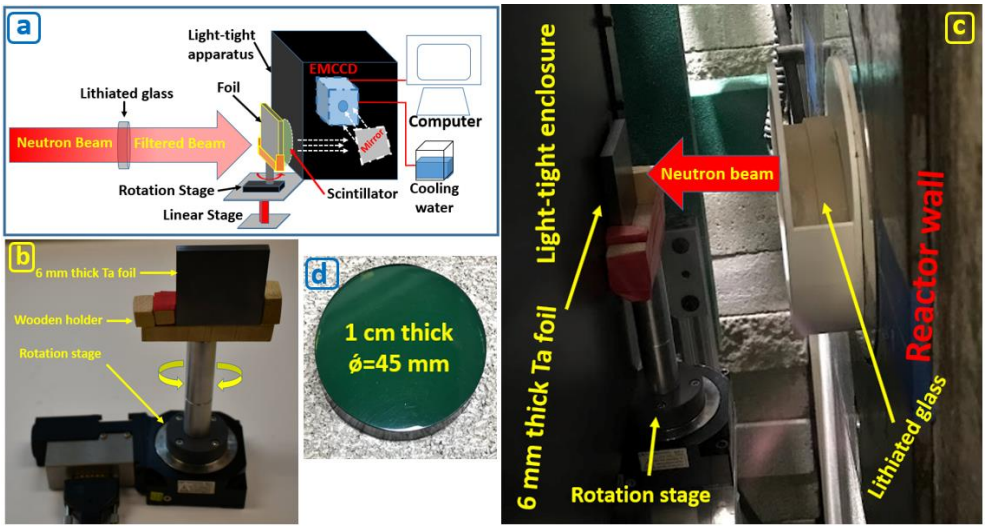

Figure 1: Schematic of the experimental set-up (a), the rotation stage with 6 mm thick Ta foil placed on a wooden holder (b), the sample mounting set up and rotation stage (c), and the HiLiY scintillator used (d).

3. RESULTS AND DISCUSSION

3.1 Factors Effecting Spatial Resolution

Before diving into the effect of test target on the system resolution, we analyze other major factors on the system resolution, including the collimation and the energy spectrum of the neutron beam, the ambient radiation field, neutron scattering within samples, type of neutron detector material and its thickness, optical paths of the camera and lens, and the post-processing of the images for noise removal. The EMCCD camera, employed in this study, has a pixel size of 16 x 16 μm^2, and a 50 mm fixed focal length lens was connected to the camera. This optical configuration provided an effective pixel size of 84 µm. Although shielding materials were placed around the camera, the imaging sensor within the camera is not completely free from the ambient neutron and gamma radiations. These interactions, especially the direct interactions of neutrons in silicon, produce

saturated pixels appearing as white spots and/or lines in the radiographs requiring post processing via digital filtering that would negatively impacts the achievable spatial resolution.

The neutron beam from the research reactor is shaped by a ~205-cm long collimator, engineered to produce a beam as parallel as possible, and with a massive beam stop weighted ~2 metric tons that comprises of neutron and gamma shielding materials to reduce the radiation dose level at the experiment area for personnel protection [12]. Any divergence or non-uniformity of the beam can cause degradation in the spatial resolution. To investigate the beam divergence, twelve radiographs of the beam profile were collected consecutively with the same image acquisition time of 1 minute but varying the distance between the beam exit and the detector (over the 2.74 – 13.74 cm range). Radiographs were post-processed by applying median filter to remove white spots/lines, and the change in the radius of each radiograph was calculated. Two of the post-processed beam profile radiographs are shown in Figure 2, with the one on the top-left taken at 12.74 cm and the one on the bottom-left obtained at 2.74 cm away from the beam exit. The radiograph acquired at the furthest distance from the beam exit is dimmer because of the loss of total neutrons as a result of beam divergence. Figure 2c shows data points (blue dots) representing a change in radius of the beam with respect to the distance from beam exit.

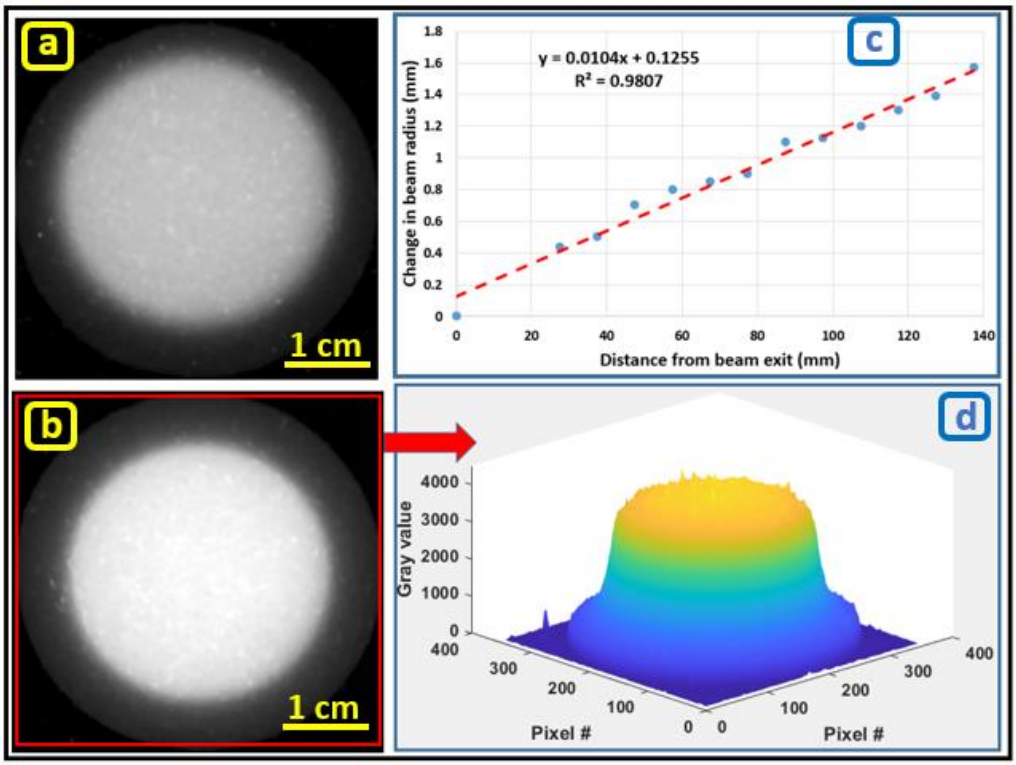

Figure 2: Open beam radiographs obtained at 12.74 cm (a) and at 2.74 cm (b) distances between scintillator and the beam exit, plot (c) showing the change in the beam radius with changing the distance from the beam exit, 2D beam profile of the radiograph taken at 2.74 cm distance (d).

The data point at (0,0) represents the initial zero increment of beam radius at beam exit where it is yet to change. A fitting process was applied to the data, and the red dashed linear fit was obtained, shown in Figure 2c. The arctangent of the slope of the fitted curve provided a beam divergence of ~0.6°. Figure 2d replot Figure 2b as the gray value in 3D profile of the radiograph in taken at the 2.74 cm distance from the beam exit, showing a relatively flat background neutron beam.

Fast neutrons deposit their energy into a medium mostly via elastic scattering. In this study, a PVT-based plastic scintillator whose chemical formula C_9H_{10} was utilized. Due to the conservation of energy and momentum, neutrons interacting elastically with protons transfer more energy into the

scintillator medium than those interacting with Carbon nuclei. The trajectory and the range of the recoiled proton in the scintillator medium are dependent on the neutron beam energy spectrum, the interaction angle, energy of the recoiled proton, and the composition of the medium. Knowing the maximum range of the recoiled proton in the vertical direction can provide information regarding the lowest limit of spatial resolution due to neutron-proton scattering in the scintillator. Therefore, to obtain the trajectory and energy of the recoiled proton (in the laboratory frame), a simplified monoenergetic 2 MeV neutron is used in the calculations according to $E_p=E_n(Cos\theta)^2$ equation at different recoil angles from 0° to 85° with an increment of 5°. To acquire the ranges of the recoiled protons, Stopping and Range of Ions in Matter (SRIM) simulations were performed in the medium of PVT [15]. Figure 3 provides vertical and horizontal ranges of protons recoiled with various angles, upon interacting with a neutron impinging on the scintillator surface perpendicularly.

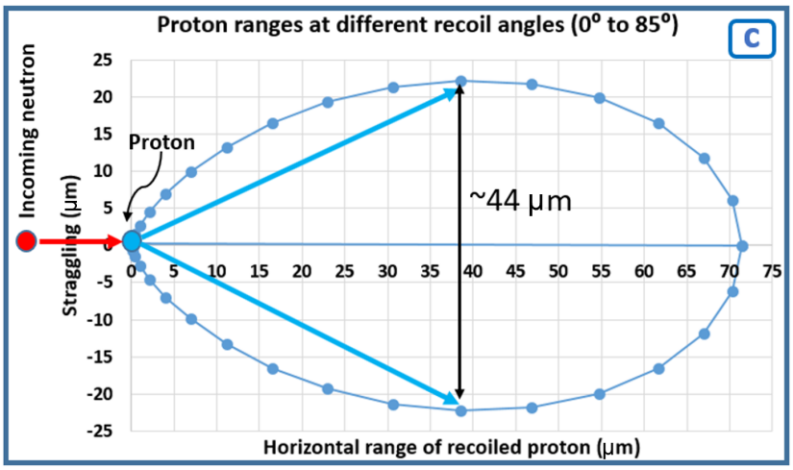

Figure 3: Ranges of protons recoiled from a 2 MeV neutron impinging perpendicularly on a PVT medium.

According to this calculation, when there is a knock-on collision, the recoil proton has a maximum horizontal range of 71.4 µm. Recoil protons at 30° have the maximum vertical range of ~22 µm,

which yields ~44 μm maximum spread when considering protons may be recoiled in both directions. This result shows that ~44 μm is the lowest theoretical value for the achievable resolution that can be achieved with 2 MeV neutrons interacting with a PVT detector, assuming no optical scattering. The lowest theoretical achievable resolution value drops to ~31 μm when considering the beam's median energy of 1.6 MeV.

Figure 4 shows another scenario in which the angle between the direction of the incoming neutron and the scintillator surface normal is 30°. In this case, the oval shape rotates counterclockwise around the interaction point, producing a ~51 μm spread in recoil protons. The spread decreases to ~47 μm when utilizing 1.6 MeV neutrons. This shows that neutrons penetrating at any angle other than normal to the scintillator surface can cause further degradation in spatial resolution.

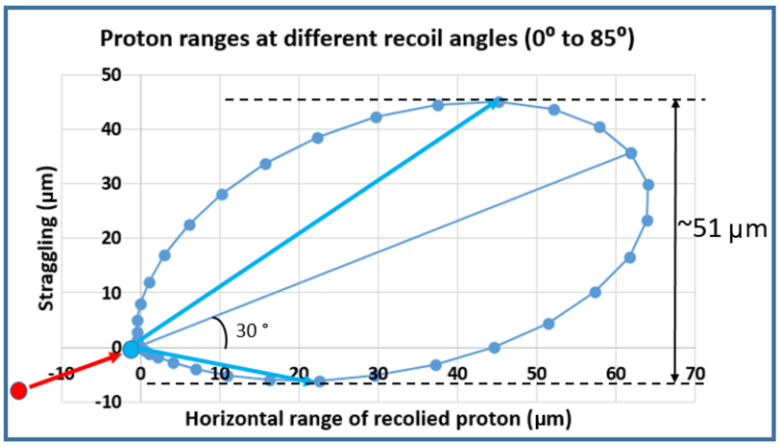

Figure 4: Ranges of protons recoiled from a 2 MeV neutron with a penetration angle of 30° between the direction of the incoming neutron and the scintillator surface normal.

Calculations and SRIM simulations show that the maximum vertical range spread is proportional to the energy of incoming neutrons. For the commonly employed 14 MeV D-T neutrons at normal

incidence on the scintillator surface, the maximum vertical range is calculated to be ~1.28 mm, which is ~56 times higher than that is obtained with 2 MeV neutrons.

3.2 Results and discussion on edge methods

To obtain the relation of MTF versus thickness of the test target, foils of 3-mm 99.99% Ta, a 6-mm 99.9% Ta and a 2.54 cm 99.95% W cube were used to acquire knife-edge radiographs. Radiographs of the edges of Ta foils and the W cube were acquired as they were placed on the wooden holder, which was connected to a rotation stage. To obtain the best alignment possible with the scintillator and the beam, the foils and the cube were stationed as parallel as possible to the scintillator, and then rotated in both clockwise and counterclockwise directions with an increment of as small as 0.1°, when the knife-edge radiographs were being collected. All radiographs were acquired with an exposure time of 120 seconds and EM gain of 20; the distance between the scintillator and the imaging target was kept at ~1 mm. Additionally, open-field and dark beam (As the beam shutter was closed, and the reactor on) images were also collected for each sample. The dark beam image was subtracted from both the open beam image and the radiograph taken with a sample. The resulting radiograph of a sample was divided by the resulting open-field beam image, then a 4-pixel median filter was applied to the final radiograph to remove electronic noise (salt and pepper noise). Furthermore, saturated pixels occasionally found, which are white spikes on the radiographs that are caused by direct hits (neutron captures and gamma rays) in the camera sensor, were removed using a median filter with varying pixel sizes depending on the severity of the saturation [16, 17]. After post-processing, edge spread functions of each set of radiographs were generated, and comparisons were made in each set to determine the best-

aligned radiograph. Figure 5 provides three edge-radiographs of 5 cm thick Ta foil obtained at -1.0°, -2.0°, and -3.0°, and the edge spread functions of red rectangular regions.

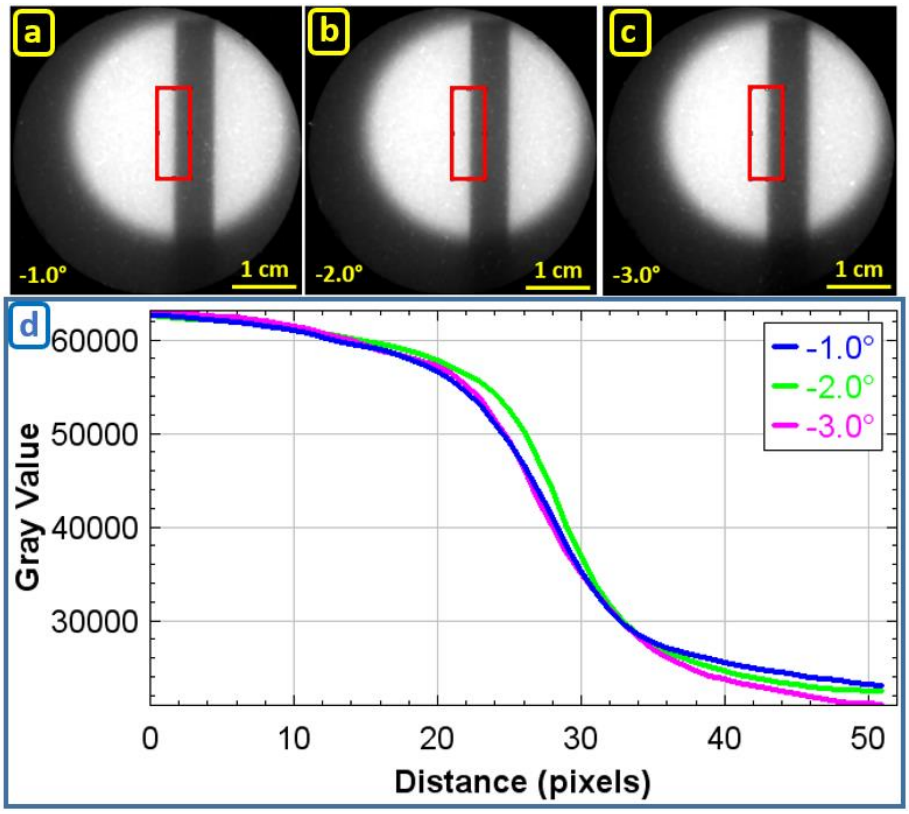

Figure 5: Knife-edge radiographs of 5 cm thick Ta foil taken at -1.0° (a), -2.0° (b), and -3.0° (c) , edge-spread functions of red rectangular regions (d).

The edge-spread functions in Figure 5d reveal that the radiograph taken at -2.0° has the best alignment, as it is otherwise impossible to differentiate with visual inspection. Figure 6 shows the photograph, the obtained knife-edge radiograph, and the edge-spread function corresponding to the red rectangular region on Figure 6-b1, b2, b3, and b4 of 3 mm, 6 mm, and 5 cm thick Ta foils and 2.54 cm thick W cube, respectively.

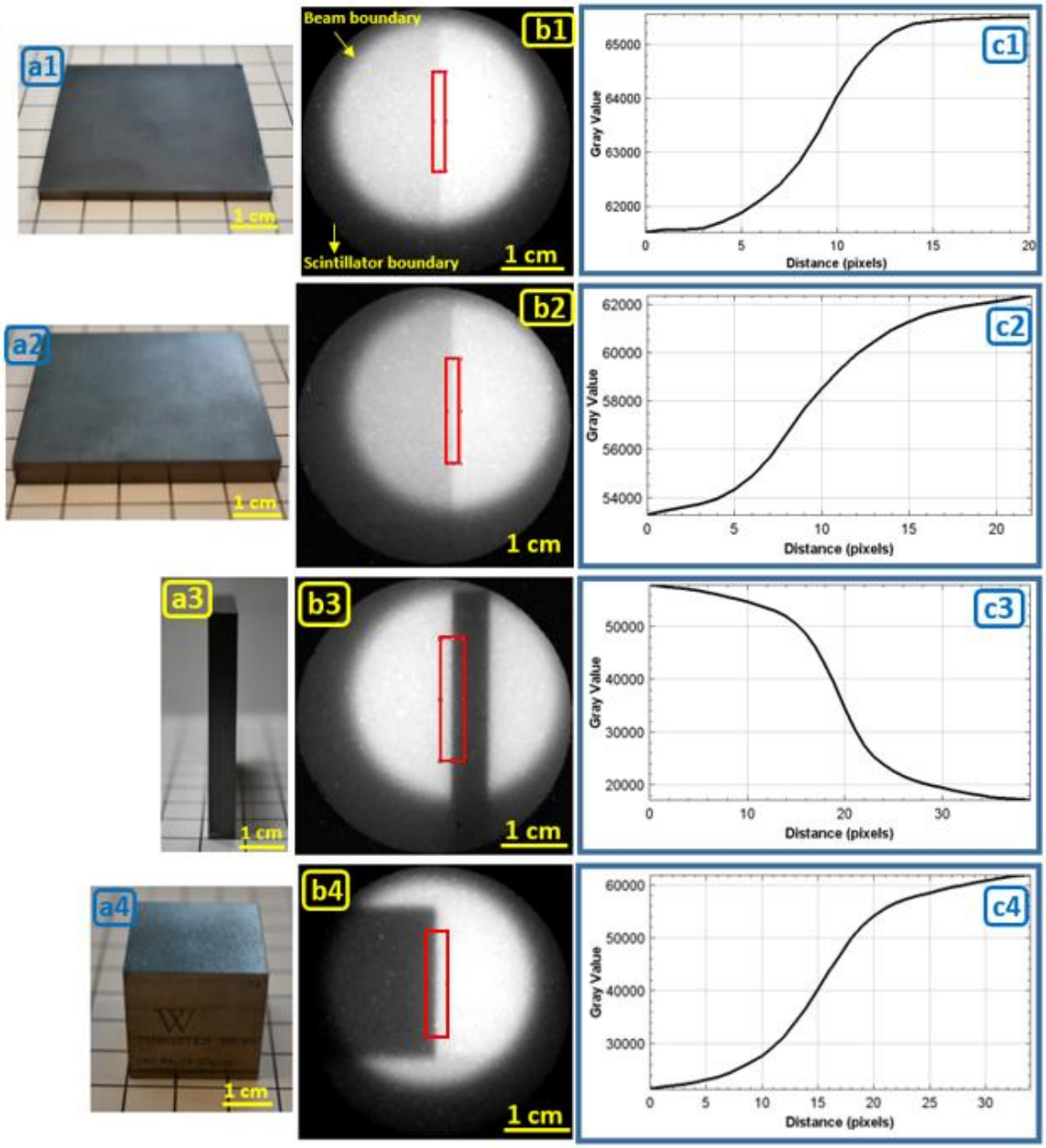

Figure 6: Photograph (a1), knife-edge radiograph (b1), and line profile crossing the red rectangular region on the knife-edge radiograph (c1) of 3 mm thick Ta foil / Photograph (a2), knife-edge radiograph (b2), and line profile crossing the red rectangular region on the knife-edge radiograph (c2) of 6 mm thick Ta foil / Photograph (a3), Knife-edge radiograph (b3), and line profile crossing the red rectangular region on the knife-edge radiograph (c3) of 5 cm thick Ta foil

/ Photograph (a4), knife-edge radiograph (b4), and line profile crossing the red rectangular region on the knife-edge radiograph (c4) of 2.54 cm thick W cube.

In radiograph (b1) in Figure 6, the left half of the beam is occluded by the 3 mm thick tantalum, blocking ~5% of the 1.6-MeV neutrons from reaching the scintillator. Beam and scintillator boundaries are also indicated by yellow arrows on the radiograph. The line profile, given in Figure 6-c1, of the region shown as red rectangular on the radiograph, provides information about how rapidly the gray value (proportional to the number of neutrons hitting the scintillator) changes at the edge of the Ta foil. The leveling off of the gray value at upper right and lower left sections in the plot represents the open beam, where there is no Ta foil covering the beam, and the beam covered by Ta foil, respectively.

Figure 6-b2 shows the knife-edge radiograph taken with 6 mm thick Ta foil. Since the thickness of the Ta foil is doubled (compared to the data shown in Figure 6-a1 from the 3 mm foil), the region where Ta foil occupies on the radiograph is darker than that of the 3 mm radiograph. This can also be seen by comparing the lowest gray values on both line profiles.

The knife-edge radiograph of the 5 cm thick Ta was acquired by aligning the 6-mm thick Ta foil parallel to the beam, in other words, to image its side which is 5 cm long. The obtained radiograph is given in Figure 6-b3. As expected, 5 cm yielded the highest contrast among all Ta foil thicknesses.

The Knife-edge radiograph of the Tungsten cube is given in Figure 6-b4. Sufficient contrast was achieved due to the thickness of the cube.

Figure 7 shows the relation between the contrast (%) calculated via ((Maximum grayscale value-Minimum grayscale value) / (Maximum grayscale value + Minimum grayscale value)) X 100, obtained from the line profiles of Ta foils and W cube and the foil/cube thickness. A linear relation between the contrast the foil/cube thickness arises because the neutron absorption becomes more probable with increasing thickness.

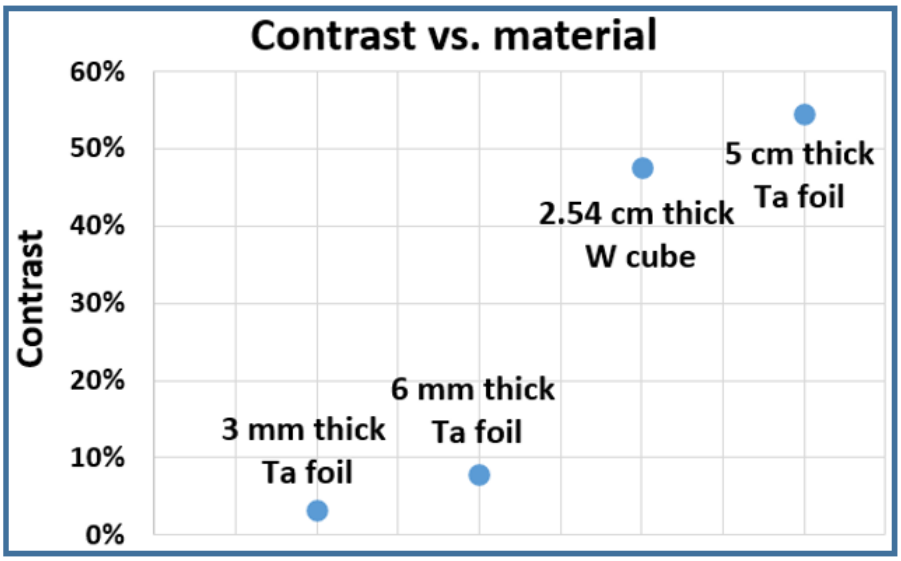

Figure 7: The difference of maximum and minimum grayscale values in the line profiles of radiographs with respect to foil/cube thickness.

Red rectangular regions on each knife-edge radiograph in Figure 6-b1, b2, b3, and b4 were cropped and uploaded into a MATLAB script, which creates the line spread function by taking the derivative of the edge-spread function and generates the modulation transfer function by applying fast Fourier transform (FFT) to the line spread function. The modulation transfer functions, shown in Figure 8, deliver information regarding spatial resolutions of knife-edge radiographs.

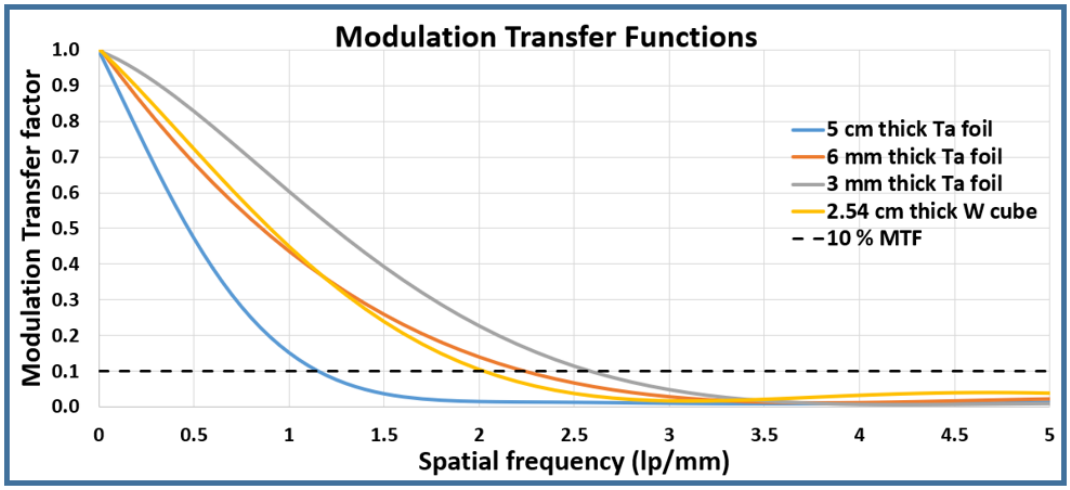

Figure 8: Modulation transfer functions of knife-edge radiographs obtained using Ta foils and W cube.

At 10% modulation transfer factor, spatial frequencies, in terms of line pair per mm, were found to be the highest and the lowest for 3 mm and 5 cm thick tantalum foils, respectively, while the spatial frequencies of 6 mm thick Ta foil and 2.54 cm thick W cube were intermediate. Spatial resolutions (SR) in units of micrometer for 10% MTF, were calculated using the equation, SR(μm)=(1/(2 x Spatial Frequency (lp/mm))) x (1000 μm /1mm), and the error in SRs, which include the calculated average standard deviation of ~2 % in pixel grayscale value and the error caused by the alignment and the beam divergence and not easily calculable, was estimated as 10 %. The SRs, as well as their errors, are provided in Figure 9.

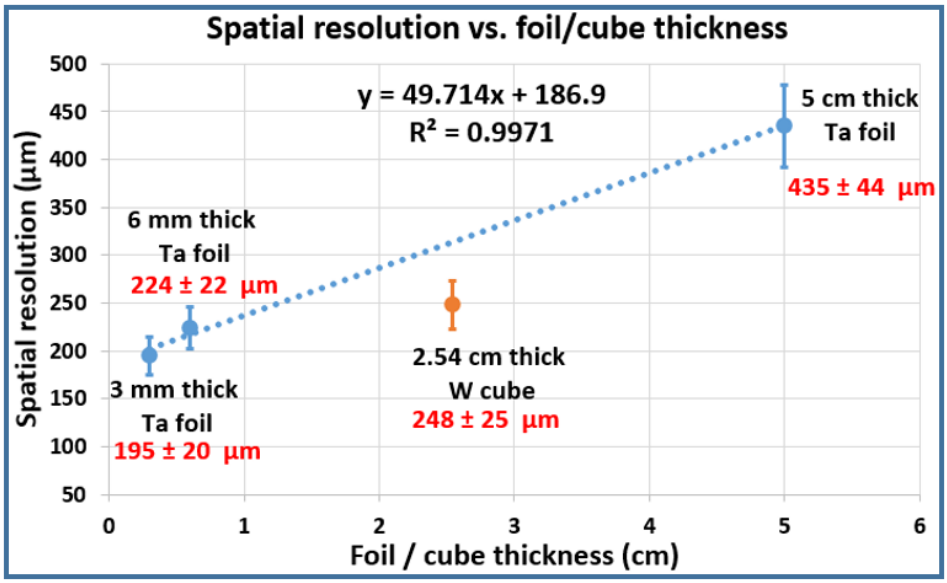

Figure 9: Spatial resolutions, with their errors, in µm, of Ta foils and W cube calculated from modulation transfer functions at 10 % MTF.

The spatial resolution degrades as the thickness of the imaging target increases. While the spatial resolution obtained with 3 mm thick Ta foil is the best, 5 cm thick Ta foil provides the worst spatial resolution, in the set. The poorest resolution for the thickest target is likely due to the effect of scattered neutrons from the imaging target even though it yields the highest contrast via neutron absorption. 6 mm thick Ta foil and 2.54 cm thick W cube may provide similar spatial resolutions when the 10 % error is considered.

There seems to be a linear relation between thickness and spatial resolution when three data points of Ta foils are considered. This linearity suggests that the 2.54 cm thick W cube would give better spatial resolution than the Ta foil with the same thickness. However, it can be seen in Figure 10 that both W and Ta with thicknesses of 2.54 cm have very similar neutron scattering across the

energies interested. Future work to collect data using Ta with thicknesses between 6 mm and 5 cm will be expected to reveal the accurate relation.

The relation between neutron scattering and thickness can also be seen in Figure 10 which shows percentages of neutron absorption and scattering in the samples being used over a neutron energy range of 0.1 MeV to 2.0 MeV.

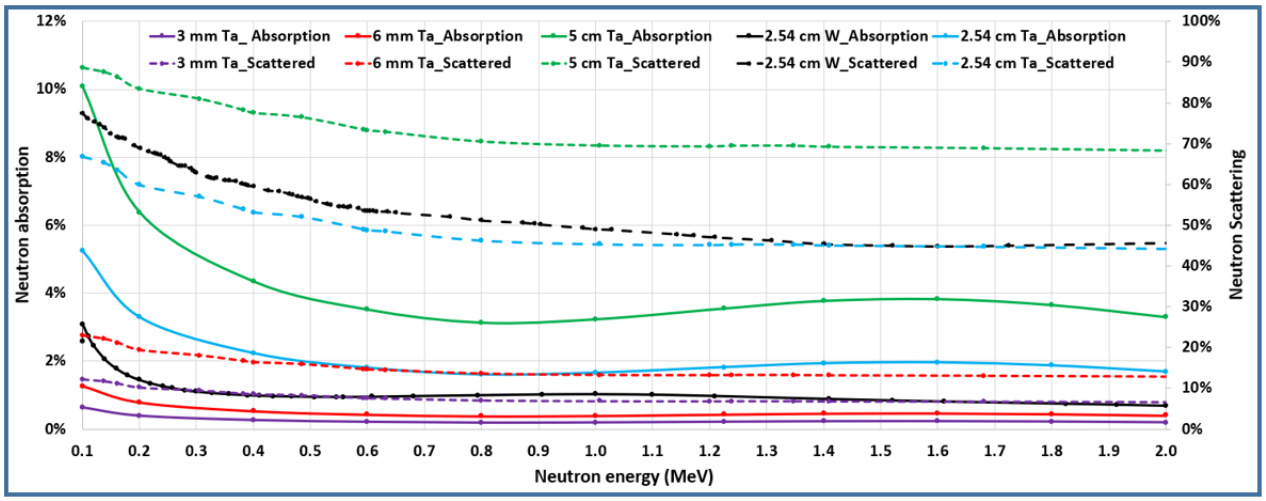

Figure 10: Neutron absorption and scattering in Ta foils and W cube spanning 0.1 – 2 MeV.

Neutron scattering is more prominent in all samples compared to absorption, and it increases with the thickness of the sample, which causes spatial resolution to deteriorate. In Ta foils, it is easier to see in the 5 cm foil data, the ratio of scattering to absorption rises with increasing energy of neutron up to ~0.8 MeV (scattering/absorption ≈ 22.5 @ 0.8 MeV), however, it decreases after this point and reaches a local minimum at ~ 1.6 MeV (scattering/absorption ≈ 18).

4. CONCLUSION

In this study, the effect of imaging target thickness on the spatial resolution was investigated at a reactor-based fast neutron beam facility using the knife-edge method. Experiments were also

conducted to determine the beam divergence, found to be a parallel beam with a divergence of ~0.6°. Knife-edge radiographs of 3 mm, 6 mm, and 5 cm Tantalum foils, and a 2.54 cm Tungsten cube were obtained, and MTF were generated. Unlike thermal or cold neutron imaging, where a thicker absorber does not drastically degrade the spatial resolution, the 10% MTF value, in μm, with tested targets are much higher (worse resolution) as a function of increasing thickness. Although the W cube is a different material than Ta foil, it provided a spatial resolution following the trend of the thickness-spatial resolution relation. SRIM simulations and calculations showed that 2 MeV neutrons, impinging on the PVT medium perpendicularly, set a limit (44 um) on the spatial resolution, and this limit increased when neutrons deviated from normal incidence. This study may pave the way for future studies on standardizing fast neutron spatial resolution measurements and enabling quantification for fast neutron screen development.

Acknowledgment: We thank the assistant from reactor staff at OSU Nuclear Reactor Laboratory and the financial support of Laboratory Directed Research and Development Program under LLNL-LDRD 20-SI-001. Work was performed under the auspices of the U.S. Department of Energy by Lawrence Livermore National Laboratory under Contract DE-AC52-07NA27344. Matt Bisbee is supported under a Department of Energy, Office of Nuclear Energy, Integrated University Program Graduate Fellowship. LLNL-JRNL-827019

References

[1] A.P. Kaestner, S. Hatmann, G. Kuhne, G. Frei, C. Grunzweig, L. Josic, F. Schmid, E.H. Lehmann, The ICON beamline - A facility for cold neutron imaging at SINQ, Nuclear Instruments and Methods in Physics Research A, 659 (387-393) (2011).

[2] M.J. Muhlbaur, T. Bucherl, M. Kellermeier, M. Knapp, M. Makowska, M. Schulz, S. Zimnik, H. Ehrenberg, Neutron imaging with fission and thermal neutrons at NECTAR at MLZ, Physics B: Condensed Matter, 551 (359-363) (2018).

[3] J.J. Rant, M. Balasko, Epithermal and fast neutron radiography using photoluminescent imaging plates and resonance and threshold activation detectors, The 12th International Conference of the Slovenian Society for Non-Destructive Testing-Application of Contemporary Non-Destructive Testing in Engineering, September 4-6, 2013, Portoroz, Slovenia.

[4] E. H. Lehmann, Neutron Imaging Facilities in a Global Context, Journal of Imaging, 3(4), 52 , (2017).

[5] H. likura, N. Tsutsui, T. Nakamura, M. Katagiri, M. Kureta, J. Kubo, M. Matsubayashi, Evaluations of the new LiF-scintillator and optional brightness enhancement films for neutron imaging, Nuclear Instruments and Methods in Physics Research A 651 (100-104) (2011).

[6] A.S Losko, Y. Han, B. Schillinger, A. Tartaglione, M. Morgano, M. Strobl, J. Long, A.S. Tremsin, M. Schulz, New perspective for neutron imaging through advanced event-mode data acquisition, Nature scientific reports, DOI: 10.1038/s41598-021-00822-5.

[7] E. H. Lehmann, D. Mannes, M. Strobl, B. Walfort, A. Losko, B. Schillinger, M. Schulz, S. C. Vogel, D. C. Schaper, D. C. Gautier, D. Newmark, Improvement in the spatial resolution for imaging with fast neutrons, Nuclear Instruments and Methods in Physics Research A, 988 (164809) (2021).

[8] I. Oksuz, W. Chuirazzi, H. P. Martinez, N. Cherepy, L. Cao, Characterization of Polyvinyl Toluene (PVT) scintillators for fast neutron imaging, SPIE Hard X-ray, Gamma-Ray, and Neutron Detector Physics XX 10762, 107620D (2018).

[9] W. Chuirazzi, I. Oksuz, P. Kandlakunta, T. N. Massey, C. R. Brune, N. J. Cherepy, H. P. Martinez, L. Cao, Evaluation of polyvinyl toluene scintillators for fast neutron imaging, Journal of Radioanalytical and Nuclear Chemistry, 318 (543-551) (2018).

[10] R. L. Cao, S. R. Biegalski, The measurement of the presampled MTF of a high spatial resolution neutron imaging system, Nuclear Instruments and Methods in Physics Research A, 582 (621-628) (2007).

[11] K. Rossmann, Measurement of the Modulation Transfer Function of Radiographic Systems Containing Fluorescent Screens, Phys. Med. Biol. 9 551 (1964).

[12] I. Oksuz, M. Van Zile, M. Bisbee, A. Kauffman, J. Hatch, P. Kandlakunta, N. J. Cherepy, L. R. Cao, Characterization of a reactor-based fast neutron beam facility for fast neutron imaging, Hard X-Ray, Gamma-ray, and Neutron Detector Physics XXII 11494, 114940T.

[13] R. D. Sanner, N. Cherepy, H. Q. Pham, V. G. Young Jr, Phosphorescent heteroleptic iridium (III) cyclometallates: Improved syntheses of acetylacetonate complexes and quantum chemical studies of their excited state properties, Polyhedron 176 (2020) 114256.

[14] N. J. Cherepy, Z. M. Seeley, S. Hok, D. Schneberk, P. Kerr, S.P. O'Neal, I. Oksuz, M. Bisbee, L. R. Cao, S.A. Payne, R. D. Sanner, G. Stone, B.F. Hobson, G. Guethlein, J. Hall, R. Stoneking, J. Mintz, C. McNamee, P.A. Thelin, Scintillator and Detectors for MeV X-ray and Neutron Imaging, Proc. SPIE 11494, Hard X-Ray, Gamma-Ray, and Neutron Detector Physics XXII, 114940N (17 September 2021).

[15] J. F. Ziegler, M. D. Ziegler, J. P. Biersack. "SRIM-The stopping and range of ions in matter (2010)." Nuclear Instruments and Methods in Physics Research Section B: Beam Interactions with Materials and Atoms 268.11-12 (2010): 1818-1823.

[16] J. Baggio, C. H'hose, M. Martinez, O. Musseau, Transient noise in a CCD camera sensor induced by neutron and gamma irradiation, 6th European Conference on Radiation and Its Effects on Components and Systems, DOI: 10.1109/RADECS.2001.1159278.

[17] A. Marbs, F. Boochs, Investigating the influence of ionizing radiation on standard CCD camera and a possible impact on photogrammetric measurements, ISPRS Commission V Symposium 'Image Engineering and Vision Metrology', ISPRS Volume XXXVI, part 5, (184-189).